JOURNAL OF GUIDANCE, CONTROL, AND DYNAMICS
Vol. 19, No. 5, September–October 1996

New Pulse-Modulation Technique for Guidance and Control of Automated Spacecraft

Sam W. Thurman*
Jet Propulsion Laboratory, California Institute of Technology, Pasadena, California 91109
and
Henryk Flashner†
University of Southern California, Los Angeles, California 90089-1453

A comprehensive approach to problems such as automated on-orbit rendezvous and soft landing on a planetary surface is presented for spacecraft employing pulse-operated (on-off) propulsion systems. Using a technique derived from robust control theory, a new class of guidance algorithms that modulate the duration and frequency of thruster firings is developed. These algorithms allow analytical characterization of transient errors, limit cycle deadband, and the set of possible terminal conditions in the design process, without the use of dynamical approximations such as linearization. With this approach, the desired performance is ensured in the presence of dynamical modeling errors with known bounds; the effects of navigational errors can be minimized to the extent that they can be bounded. A realistic application is illustrated via computer simulation of a hypothetical mission scenario, in which a robotic spacecraft equipped with an aided-inertial guidance system soft lands on the planet Mars.

Introduction

IN missions carried out with robotic spacecraft, self-contained guidance and control are often desirable and in some cases a necessity. Although a wealth of theory exists for applications such as automated orbital transfer, rendezvous, station keeping, and soft landing, among others, much of this knowledge base presumes the use of continuous throttleable or fixed-thrust propulsion, whereas in practice many spacecraft are equipped with on-off gas jets or thrusters because of their relative simplicity and low cost. This paper describes a new technique for pulse-modulated operation of these devices intended for use in the aforementioned problems.

A representative, but not exhaustive, review of previous work emphasizing mission applications is as follows. Much of the rendezvous literature is devoted to the determination of optimal trajectories and their associated thrust profiles. Both theoretical and operational aspects of rendezvous are discussed in the survey papers by Jezewski et al.[1] and Leonard and Bergmann.[2] Parten and Mayer[3] and Young and Alexander[4] describe the rendezvous and docking procedures developed for the Gemini and Apollo piloted missions, respectively; these procedures have also been used in Space Shuttle missions. Automated rendezvous schemes have been proposed for the Space Shuttle[5,6] but not implemented. Previous missions involving soft landing have all been accomplished with throttleable propulsion systems. The early work leading to the guidance algorithms used in the Apollo missions was performed by Cherry[7] and Battin.[8] The operational Apollo lunar module guidance system is described by Klumpp.[9] The automated guidance schemes used by the Surveyor and Viking spacecraft were similar: the terminal descent system developed for the Surveyor lunar lander is described by Cheng et al.,[10] and Ingoldby[11] discusses the corresponding system for the Viking Mars landers.

Another prevalent feature of the literature is the use of linear approximations of the spacecraft's dynamics to obtain an analytically tractable problem. Given the nonlinear behavior of on-off thrusters, the closed-loop dynamics of systems employing these devices will be nonlinear even in cases where the spacecraft dynamics are otherwise linear. The use of on-off thrusters for attitude control and station keeping presents similar problems. Control system design in these cases has been accomplished with phase-plane analysis and detailed computer simulation (e.g., the attitude control scheme of Farrenkopf et al.[12]). The autopilot systems for the Apollo lunar module,[13] the Viking lander,[11] and the Space Shuttle[14] have all employed phase-plane switching logic of some form. In the approach employed herein, the guidance problem is solved with an extension of the robust nonlinear control theory of Corless[15] and Leitmann,[16] without the use of linear approximations or phase-plane diagrams. The solution yields a new class of pulse-width/pulse-frequency modulation algorithms that result in a quasilinear closed-loop system. These algorithms allow for analytical characterization of transient error behavior, limit cycle deadband, and the domain of possible terminal states. Furthermore, it is shown that a prescribed response is obtained in the presence of bounded dynamical modeling errors and navigational errors.

Problem Description

A general form for the differential equations governing the motion of a space vehicle with mass $m(t)$ that is useful in rendezvous, soft landing, and station keeping applications is as follows:

$$m(t)\ddot{\boldsymbol{r}}(t) = m(t)\boldsymbol{g}[\boldsymbol{r}(t), \boldsymbol{r}_O(t)] + m(t)\boldsymbol{c}[\boldsymbol{r}(t), \dot{\boldsymbol{r}}(t), \boldsymbol{\omega}_F(t), \dot{\boldsymbol{\omega}}_F(t)] + \boldsymbol{f}_T(t) \quad (1)$$

Equation (1) assumes a coordinate frame with its origin at some point O, that rotates with angular velocity $\boldsymbol{\omega}_F$ in inertial space. The three-dimensional vectors $\boldsymbol{r}$, $\dot{\boldsymbol{r}}$, and $\ddot{\boldsymbol{r}}$ denote the position, velocity, and acceleration of the spacecraft, respectively, in the rotating frame. The position of the origin, O, in an inertial frame is given by the vector $\boldsymbol{r}_O$. The vector functions $\boldsymbol{g}$ and $\boldsymbol{c}$ represent gravitational acceleration and Coriolis effects, respectively. The vector function $\boldsymbol{f}_T$ represents the applied thrust force. For orbital rendezvous problems, the point O is chosen to be the location of the target spacecraft; the rotating coordinate frame is aligned with $\boldsymbol{r}_O$, taken to be the position of the target vehicle relative to the center of the attracting body, and rotates with $\boldsymbol{r}_O$. The same arrangement is also applicable to the station keeping problem: in this case $\boldsymbol{r}_O$ defines the desired orbit profile to be maintained. In terminal descent problems, the vector $\boldsymbol{r}_O$ specifies the target landing site, with the angular velocity of the rotating frame, ω_F, representing the rotation rate of the target body. An illustration of this type of coordinate frame for the terminal descent application is given in Fig. 1.

Received Nov. 28, 1994; revision received March 11, 1996; accepted for publication March 13, 1996.

*Member, Technical Staff, Flight Systems Engineering Section, Systems Division, 4800 Oak Grove Drive. Senior Member AIAA.

†Associate Professor, Department of Mechanical and Aerospace Engineering, University Park. Member AIAA.

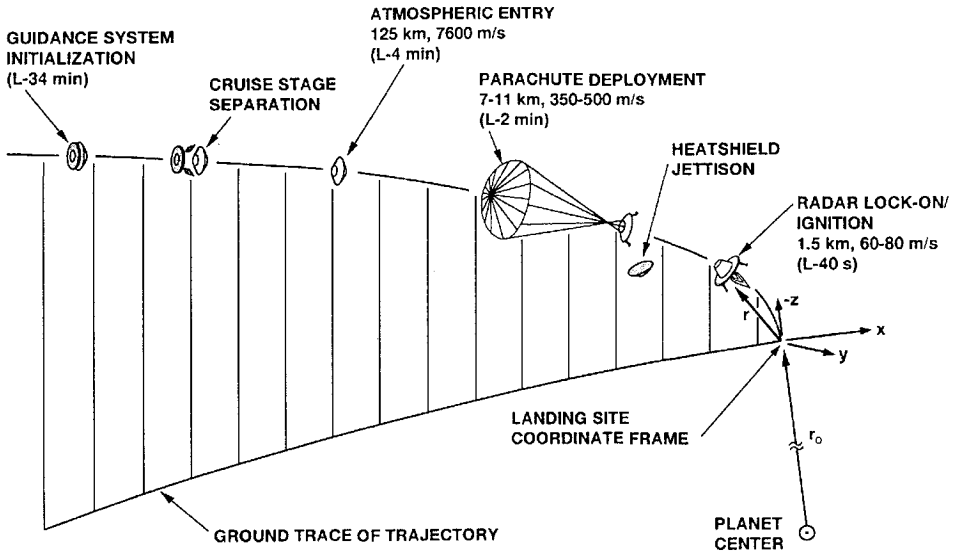

Fig. 1 Mars lander mission profile.

To perform a rendezvous, the relative position and velocity of the spacecraft must be simultaneously reduced to values small enough to permit successful docking with the target vehicle. A soft landing mission also requires simultaneous control of position and velocity, relative to a planetary surface. Station keeping, or orbit maintenance, is a logical extension of rendezvous, in which the station keeping spacecraft must essentially rendezvous with the desired orbit profile repeatedly. These mission types are all conceptually similar from the standpoint of guidance.

In many cases it is desired not only to control the terminal state vector of the spacecraft but also to have it follow a desired trajectory profile to meet additional mission constraints. A more general version of Eq. (1) that accommodates this situation is given next. The six-dimensional spacecraft state vector is recast in terms of the guidance error vector $\boldsymbol{x}$ defined as

$$\boldsymbol{x}(t) = \begin{bmatrix} \boldsymbol{r}(t) - \boldsymbol{r}_d(t) \\ \dot{\boldsymbol{r}}(t) - \dot{\boldsymbol{r}}_d(t) \end{bmatrix} \tag{2}$$

In Eq. (2), $\boldsymbol{r}_d(t)$ and $\dot{\boldsymbol{r}}_d(t)$ represent the desired position and velocity profile of the spacecraft, respectively. Incorporating Eq. (2) into Eq.(1) yields the following differential equation for $\boldsymbol{x}$:

$$\dot{\boldsymbol{x}} = \boldsymbol{A}\boldsymbol{x} + \boldsymbol{B}[\boldsymbol{g}(\boldsymbol{r}, \boldsymbol{r}_O) + \boldsymbol{c}(\boldsymbol{r}, \dot{\boldsymbol{r}}, \omega_F, \dot{\omega}_F) - \ddot{\boldsymbol{r}}_d + \boldsymbol{a}_T] \tag{3}$$

where

$$\boldsymbol{A} = \begin{bmatrix} \boldsymbol{0} & \boldsymbol{I} \\ \boldsymbol{0} & \boldsymbol{0} \end{bmatrix}, \qquad \boldsymbol{B} = \begin{bmatrix} \boldsymbol{0} \\ \boldsymbol{I} \end{bmatrix} \tag{4}$$

In Eq. (3), the vector $\boldsymbol{a}_T$ is the thrust acceleration, which is equal to $f_T(t)/m(t)$, and in Eq. (4), $\boldsymbol{I}$ is the 3×3 identity matrix. For autonomous operation, a function of the form $f_T = f(\boldsymbol{r}_d, \boldsymbol{x})$ specifying the commanded thrust vector that will yield some desired closed-loop system is sought.

Pulse-Modulation Guidance Theory

For pulse-operated propulsion systems, guidance equations are needed that determine thrust vector magnitude and orientation commands and provide the logic for their implementation. In this section a class of guidance equations applicable to two different thruster configurations is developed.

Analysis

The proposed class of functions for the commanded thrust vector, which shall be designated f_c, consists of three components, as follows:

$$f_c = f_O(\boldsymbol{r}_d, \dot{\boldsymbol{r}}_d, \ddot{\boldsymbol{r}}_d, \boldsymbol{r}_O, \omega_F, \dot{\omega}_F, \boldsymbol{x}) + f_f(\boldsymbol{x}) + f_\varepsilon(\boldsymbol{x}) \tag{5}$$

The first component f_O consists of feedback linearization terms that transform the original nonlinear system given by Eq. (3) into a nominally linear system:

$$f_O = m\ddot{\boldsymbol{r}}_d - m[\boldsymbol{g}(\boldsymbol{r}_O, \boldsymbol{r}_d, \boldsymbol{x}) + \boldsymbol{c}(\boldsymbol{r}_d, \dot{\boldsymbol{r}}_d, \omega_F, \dot{\omega}_F, \boldsymbol{x})] \tag{6}$$

Note that the second term is optional. The form of control law presented in the following remains the same, although the numerical values of the control effort and various stabilty will be different. The second component f_f is a linear feedback law designed to shape the closed-loop response of the transformed system such that it will exhibit a prescribed behavior in the absence of perturbations:

$$f_f = -m\boldsymbol{K}\boldsymbol{x} \tag{7}$$

The third component f_ε is designed to simultaneously compensate for errors as a result of thrust mechanization with discrete thruster firings and other mismodeling of the spacecraft dynamics:

$$f_\varepsilon = -mk(\boldsymbol{x}, t)\boldsymbol{n}[(1/\varepsilon)\boldsymbol{u}(\boldsymbol{x})] \tag{8}$$

The scalar function k and the vector functions $\boldsymbol{n}$ and $\boldsymbol{u}$ appearing in Eq. (8) are to be defined in the design process; the requirements they must satisfy are described in further detail later. In the most general sense, a matrix function $\boldsymbol{K}_\varepsilon$ can be used instead of k; here it is assumed for simplicity that $\boldsymbol{K}_\varepsilon = k\boldsymbol{I}$, where $\boldsymbol{I}$ is the 3×3 identity matrix. The scalar parameter ε in Eq. (8) ultimately determines the accuracy with which the closed-loop system approximates the desired linear system and will also be discussed subsequently.

In practice quantities such as the spacecraft position and velocity are not known precisely but are estimated by an onboard navigation system and other sensors. Other parameters, such as the spacecraft mass, are not estimated but are known to fall within some bounded range. The commanded thrust components given in Eqs. (6–8) are therefore computed as follows:

$$f_c = \hat{m}\{\ddot{\boldsymbol{r}}_d - \hat{\boldsymbol{g}}(\hat{\boldsymbol{r}}_O, \boldsymbol{r}_d, \hat{\boldsymbol{x}}) - \hat{\boldsymbol{c}}(\boldsymbol{r}_d, \dot{\boldsymbol{r}}_d, \dot{\omega}_F, \hat{\boldsymbol{x}}) - \boldsymbol{K}\hat{\boldsymbol{x}} - k(\hat{\boldsymbol{x}}, t)\boldsymbol{n}[(1/\varepsilon)\boldsymbol{u}(\hat{\boldsymbol{x}})]\} \tag{9}$$

In Eq. (9), $\boldsymbol{x}$, $\boldsymbol{r}_O$, and m are denoted with hat symbols to indicate the use of inexact estimates or nominal values for these parameters. The derivative of ω_F is not shown in Eq. (9) because both it and ω_F can be computed from $\boldsymbol{r}_O$ in rendezvous and station keeping applications, and in soft landing applications ω_F is very nearly constant for most target bodies of interest.

The actual thrust force at any instant will differ from the commanded value, with the extent of this difference depending primarily

on the number of discrete thrust levels available from the spacecraft's propulsion system. The applied thrust vector $\boldsymbol{f}_T$ is

$$\boldsymbol{f}_T = \boldsymbol{C}\delta\boldsymbol{C}\left[\boldsymbol{C}^T\boldsymbol{f}_c + \delta\boldsymbol{f}_m^b\right] \tag{10}$$

In Eq. (10), the matrix $\boldsymbol{C}$ is the orthogonal transformation matrix between the spacecraft body-fixed reference frame mechanized in the spacecraft's computer and the rotating frame used for the guidance computations. The matrix $\delta\boldsymbol{C}$ is the transformation matrix between the true spacecraft body frame and the computed body frame. The vector $\delta\boldsymbol{f}_m$ represents the applied thrust error as a result of quantization and any other types of thrust mechanization errors. The use of superscript b in Eq. (10) denotes that the indicated vector is expressed in the body frame. If it is assumed that the attitude determination errors embodied in the matrix $\delta\boldsymbol{C}$ are small (on the order of a few degrees), then $\delta\boldsymbol{C}$ can be accurately approximated as

$$\delta\boldsymbol{C} \approx \boldsymbol{I} + \delta\Theta \tag{11}$$

where

$$\delta\Theta = \begin{bmatrix} 0 & \delta\theta_z & -\delta\theta_y \\ -\delta\theta_z & 0 & \delta\theta_x \\ \delta\theta_y & -\delta\theta_x & 0 \end{bmatrix} \tag{12}$$

In Eq. (12), the parameters $\delta\theta_x$, $\delta\theta_y$, and $\delta\theta_z$ are small rotations about the x, y, and z computed body axes, respectively, which would bring the computed body frame into alignment with the true body frame. Using Eqs. (11) and (12), one can write the applied thrust vector as follows:

$$\boldsymbol{f}_T = \boldsymbol{f}_c + \delta\boldsymbol{f}_T \tag{13}$$

where

$$\delta\boldsymbol{f}_T \approx \boldsymbol{C}\delta\Theta\boldsymbol{C}^T\boldsymbol{f}_c + \boldsymbol{C}(\boldsymbol{I} + \delta\Theta)\delta\boldsymbol{f}_m^b \tag{14}$$

Further characterization of $\delta\boldsymbol{f}_m$ requires specific information about the number, thrust levels, and configuration of the thrusters comprising the propulsion system.

Using Eqs. (3), (4), (9), and (11–14), one can write the closed-loop dynamical equations of the spacecraft as follows:

$$\dot{\boldsymbol{x}} = \boldsymbol{A}\boldsymbol{x} + \boldsymbol{B}\{\delta\boldsymbol{g} + \delta\boldsymbol{c} + (\delta\boldsymbol{f}_T/m) - (\delta m/m)\boldsymbol{f}_c - \boldsymbol{K}\hat{\boldsymbol{x}} - k(\hat{\boldsymbol{x}}, t)\boldsymbol{n}[(1/\varepsilon)\boldsymbol{u}(\hat{\boldsymbol{x}})]\} \tag{15}$$

In Eq. (15), the quantities $\delta\boldsymbol{g}$, $\delta\boldsymbol{c}$, and δm are equal to $\boldsymbol{g} - \hat{\boldsymbol{g}}$, $\boldsymbol{c} - \hat{\boldsymbol{c}}$, and $m - \hat{m}$, respectively. With further manipulation, Eq. (15) can be written as

$$\dot{\boldsymbol{x}} = [\boldsymbol{A} - \boldsymbol{B}\boldsymbol{K}]\boldsymbol{x} + \boldsymbol{B}\{\delta\boldsymbol{e} - k(\hat{\boldsymbol{x}}, t)\boldsymbol{n}[(1/\varepsilon)\boldsymbol{u}(\hat{\boldsymbol{x}})]\} \tag{16}$$

where

$$\delta\boldsymbol{e} = \delta\boldsymbol{g} + \delta\boldsymbol{c} + \boldsymbol{K}\delta\boldsymbol{x} + (\delta\boldsymbol{f}_T - \delta m\boldsymbol{f}_c)/m \tag{17}$$

In Eq. (17), the vector $\delta\boldsymbol{x}$ is equal to $\boldsymbol{x} - \hat{\boldsymbol{x}}$ and represents errors in the position and velocity estimates supplied by the spacecraft's navigation system.

Equations (16) and (17) represent a nonlinear, nonautonomous system. The functions k, $\boldsymbol{n}$, and $\boldsymbol{u}$ and the parameter ε, comprising the $\boldsymbol{f}_\varepsilon$ component of the commanded thrust given in Eq. (8), ensure that the desired linear response is achieved. This is accomplished with a technique developed by Corless[15] and Leitmann[16] for use with control actuators possessing a continuous and unbounded operating range, in which modeling uncertainties are treated in a deterministic, rather than a stochastic, manner. The key extension of their theory employed herein is the use of $\boldsymbol{f}_\varepsilon$ to compensate for known thrust mechanization errors caused by the use of pulse-operated thrusters, as well as other unknown modeling errors.

The properties required of k, $\boldsymbol{n}$, and $\boldsymbol{u}$ are now stated. The function k is a positive, continuous, bounding function that must satisfy the following inequality:

$$k(\hat{\boldsymbol{x}}, t) \geq |\delta\boldsymbol{e}| \tag{18}$$

For the general case mentioned earlier, in which a matrix function $\boldsymbol{K}_\varepsilon$ is used instead of a scalar function k, Eq. (18) would be interpreted as requiring the norm of $\boldsymbol{K}_\varepsilon$ to be greater than the magnitude, or formally the Euclidean norm, of the vector $\delta\boldsymbol{e}$. The vector function $\boldsymbol{n}$ can be any continuous function with the following properties:

$$\|\boldsymbol{u}\|\boldsymbol{n}(\varepsilon, \boldsymbol{u}) = \|\boldsymbol{n}(\varepsilon, \boldsymbol{u})\|\boldsymbol{u} \tag{19a}$$

$$\|\boldsymbol{n}(\varepsilon, \boldsymbol{u})\| \geq 1 - \varepsilon/\|\boldsymbol{u}\|; \qquad \|\boldsymbol{u}\| > \varepsilon \tag{19b}$$

The vector function $\boldsymbol{u}$ is a linear function of the estimated guidance error vector $\hat{\boldsymbol{x}}$ and another feedback matrix, designated $\boldsymbol{P}$:

$$\boldsymbol{u} = \boldsymbol{B}^T\boldsymbol{P}\hat{\boldsymbol{x}} \tag{20}$$

The matrix $\boldsymbol{P}$ is obtained from the Lyapunov equation given in Eq. (21). This equation has a unique solution that is symmetric and positive definite, provided that the matrix $[\boldsymbol{A} - \boldsymbol{B}\boldsymbol{K} + \alpha\boldsymbol{I}]$ has eigenvalues with only negative real parts, where α is a positive number such that $-\alpha$ is greater than the real parts of the eigenvalues of $[\boldsymbol{A} - \boldsymbol{B}\boldsymbol{K}]$.[18,19] The matrix $\boldsymbol{Q}$ can be any positive definite matrix:

$$\boldsymbol{P}[\boldsymbol{A} - \boldsymbol{B}\boldsymbol{K} + \alpha\boldsymbol{I}] + [\boldsymbol{A} - \boldsymbol{B}\boldsymbol{K} + \alpha\boldsymbol{I}]^T\boldsymbol{P} + 2\boldsymbol{Q} = 0 \tag{21}$$

The stability of the closed-loop system defined by Eqs. (16–21) will be evaluated using Lyapunov methods.[15–19] A Lyapunov function candidate is sought that indicates that in some region of the domain of $\boldsymbol{x}$ all trajectories $\boldsymbol{x}(t)$ are uniformly exponentially convergent to within a small region of radius b (i.e., $\|\boldsymbol{x}\| \leq b$) around the origin ($\boldsymbol{x} = 0$). Specifically, this system is exponentially convergent with rate α if for some positive constant β the following inequality is satisfied[15]:

$$\|\boldsymbol{x}(t)\| \leq b + \beta\|\boldsymbol{x}(t_O)\| \exp[-\alpha(t - t_O)]; \qquad t \geq t_O \tag{22}$$

Let $V(\boldsymbol{x}) = \frac{1}{2}\boldsymbol{x}^T\boldsymbol{P}\boldsymbol{x}$, where the matrix $\boldsymbol{P}$ is obtained from Eq. (21), be Lyapunov function candidate. To validate Eq. (22), $V(\boldsymbol{x})$ must possess the following properties:

$$c_1\|\boldsymbol{x}\|^2 \leq V(\boldsymbol{x}) \leq c_2\|\boldsymbol{x}\|^2; \qquad c_1, c_2 > 0 \tag{23a}$$

$$\dot{V}(\boldsymbol{x}) \leq -2\alpha[V(x) - V^*]; \qquad V(\boldsymbol{x}) > V^* \tag{23b}$$

Equation (23) represents a set of sufficient conditions only. The fact that a Lyapunov function satisfying these conditions may not be found, or if for a given $V(\boldsymbol{x})$ these conditions are violated for some value of $\boldsymbol{x}$, does not by itself demonstrate that the origin of the closed-loop system is unstable. Equation (23a) is satisfied if $\boldsymbol{P}$ is positive definite, which is the case because $\boldsymbol{P}$ is the solution of Eq. (21). If the condition of Eq. (23b) is met, then Eq. (22) will hold, with the radius of convergence b being equal to $(V^*/c_1)^{1/2}$. Once the state vector has entered the region $\|\boldsymbol{x}\| \leq b$, it will remain within that region indefinitely. A detailed proof of these properties has been performed by Corless.[20] Equations (16) and (20) and the conditions imposed on the function $\boldsymbol{n}$ in Eq. (19) yield the following expression for $V(\boldsymbol{x})$[21]:

$$\dot{V}(\boldsymbol{x}) = -2\alpha V(\boldsymbol{x}) - \boldsymbol{x}^T\boldsymbol{Q}\boldsymbol{x} + \|\hat{\boldsymbol{u}}\|[\delta\boldsymbol{e} \cdot (\hat{\boldsymbol{u}}/\|\hat{\boldsymbol{u}}\|) - k\|\boldsymbol{n}\|] + \delta\boldsymbol{u} \cdot [\delta\boldsymbol{e} - k\|\boldsymbol{n}\|(\hat{\boldsymbol{u}}/\|\hat{\boldsymbol{u}}\|)] \tag{24}$$

If the direction of $\delta\boldsymbol{u}$ relative to $\hat{\boldsymbol{u}}$ is assumed to be arbitrary, then the following inequality can be constructed from Eq. (24):

$$\dot{V}(\boldsymbol{x}) \leq -2\alpha V(\boldsymbol{x}) + E \tag{25}$$

where

$$E \leq \|\hat{\boldsymbol{u}}\|(\|\delta\boldsymbol{e}\| - k\|\boldsymbol{n}\|) + \|\delta\boldsymbol{u}\|(\|\delta\boldsymbol{e}\| + k\|n\|) \tag{26}$$

Using the minimum requirements on k and $\|\boldsymbol{n}\|$ given in Eq. (18) and Eq. (19a), respectively, another inequality that illustrates the dependence of the region of convergence on k, $\boldsymbol{n}$, and ε is given by

$$E \leq k\varepsilon(1 + \|\delta\boldsymbol{u}\|/\|\hat{\boldsymbol{u}}\|) + \|\delta\boldsymbol{u}\|(\|\delta\boldsymbol{e}\| + k) \tag{27}$$

By establishing bounds on the terms in Eq. (27), an upper bound on E can be established. This, in turn, allows a suitable value of V^* to be determined using Eqs. (23), and hence the radius of convergence b around the origin. The second term of Eq. (27) shows that navigational errors, which manifest themselves in $\delta \boldsymbol{u}$, impose a fundamental limitation on the smallest value of E that can be achieved in practice. In some situations this limitation may be less pronounced, depending on the relative orientation of the $\delta \boldsymbol{u}$ and $\hat{\boldsymbol{u}}$ vectors over the course of the mission. Navigational data generated with a minimum variance estimation algorithm such as the Kalman filter have the property $\delta \boldsymbol{x} \cdot \hat{\boldsymbol{x}} = 0$ (see Brown,[22] for example), which in turn limits the magnitude of $\delta \boldsymbol{u} \cdot \hat{\boldsymbol{u}}$.

It should be noted that the theory just presented provides a sufficiently general framework for the synthesis of both explicit and implicit guidance laws. By making the vectors $\boldsymbol{r}_d$ and $\dot{\boldsymbol{r}}_d$ constant, with $\ddot{\boldsymbol{r}}_d = 0$, an explicit guidance law is obtained, in which the commanded thrust is a function only of the difference between the current estimated spacecraft position and velocity and the desired terminal state, specified by $\boldsymbol{r}_d$ and $\dot{\boldsymbol{r}}_d$. An implicit guidance law, in which the commanded thrust is derived from differences between the estimated flight path and a desired trajectory profile, is obtained when $\boldsymbol{r}_d$, $\dot{\boldsymbol{r}}_d$, and $\ddot{\boldsymbol{r}}_d$ are chosen to be time-varying quantities.

Reaction Control System Configuration

A guidance law for use with a reaction control system of small thrusters is illustrated next. This type of system, used for attitude control, station keeping, and small (<10–20-m/s) maneuvers, provides a fixed thrust level in each of three orthogonal directions, in both a positive and negative sense. Some spacecraft, such as the Space Shuttle, carry enough thrusters to provide two or three different thrust levels along each axis. Equations (26) and (27) will be used to characterize the behavior of state trajectories in different regions of the domain of $\boldsymbol{x}$. This presentation is a more general version of a similar guidance law developed previously by the authors.[23] We emphasize that the control law derived here does not assume orthogonal jets, and indeed the jets in the simulation example are not orthogonal.

Guidance Law

The relationship between the commanded and applied thrust for each axis of a three-axis system is shown in Fig. 2. The hysteresis behavior that is characteristic of actual thrusters is also shown in Fig. 2. The $\boldsymbol{f}_O$ component of the commanded thrust vector is as given in Eq. (9). The $\boldsymbol{f}_f$ component of the commanded thrust is a proportional-plus-derivative feedback law, as follows:

$$\boldsymbol{f}_f = -m(K_P \Delta \hat{\boldsymbol{r}} + K_D \Delta \hat{\boldsymbol{v}}) \tag{28}$$

In Eq. (28), $\Delta \hat{\boldsymbol{r}}$ and $\Delta \hat{\boldsymbol{v}}$ comprise the estimate of the guidance error vector $\boldsymbol{x}$ (i.e., $\hat{\boldsymbol{x}} = [\Delta \hat{\boldsymbol{r}} \Delta \hat{\boldsymbol{v}}]^T$). From Fig. 2, the maximum error between the commanded and applied thrust before saturation is seen to be $0.5T$. Assuming that the other error sources in Eq. (17) are small, then $\|\delta \boldsymbol{e}\| \leq T/2m$ (m in this case is the maximum spacecraft mass), and for the $\boldsymbol{f}_\varepsilon$ component of commanded thrust, the function k is also $T/2m$. The function $\boldsymbol{n}$ is

$$\begin{aligned} \boldsymbol{n}(\varepsilon, \hat{\boldsymbol{u}}) &= 0; \qquad \|\hat{\boldsymbol{u}}\| < \varepsilon \\ \boldsymbol{n}(\varepsilon, \hat{\boldsymbol{u}}) &= \hat{\boldsymbol{u}}/\|\hat{\boldsymbol{u}}\|; \qquad \|\hat{\boldsymbol{u}}\| \geq \varepsilon \end{aligned} \tag{29}$$

This form for $\boldsymbol{n}$ is chosen because it closely mimics the behavior of the thrusters. The vector $\hat{\boldsymbol{u}}$ is composed of the same feedback law used for $\boldsymbol{f}_f$ in Eq. (31):

$$\hat{\boldsymbol{u}} = K_P \Delta \hat{\boldsymbol{r}} + K_D \Delta \hat{\boldsymbol{v}} \tag{30}$$

The Appendix describes a method for deriving feedback laws of this form from Eq. (21) by substituting $\boldsymbol{B}^T \boldsymbol{P}$ for the matrix $\boldsymbol{K}$. In summary, the commanded thrust vector is

$$\begin{aligned} \boldsymbol{f}_c = m(&\ddot{\boldsymbol{r}}_d - \hat{\boldsymbol{g}} - \hat{\boldsymbol{c}} - K_P \Delta \hat{\boldsymbol{r}} - K_D \Delta \hat{\boldsymbol{v}}) \\ &- (T/2)\boldsymbol{n}[(1/\varepsilon)(K_P \Delta \hat{\boldsymbol{r}} + K_D \Delta \hat{\boldsymbol{v}})] \end{aligned} \tag{31}$$

Sensor Uncertainty Region

The existence of navigation errors will result in a region around the origin that cannot be reached with certainty. Equation (27) shows that E has a lower bound as follows:

$$E \leq \|\delta \boldsymbol{u}\|(T/m) \tag{32}$$

Using Eqs. (25) and (32), an expression defining this region can be obtained. An additional expression is needed (obtained from the Appendix), which bounds the Lyapunov function $V(\boldsymbol{x})$:

$$\begin{aligned} K_L \|\Delta \boldsymbol{r}\|^2 + K_D \|\Delta \boldsymbol{v}\|^2 - 2K_P K_D \|\Delta \boldsymbol{r}\| \|\Delta \boldsymbol{v}\| \leq V(\boldsymbol{x}) \\ \leq K_L \|\Delta \boldsymbol{r}\|^2 + K_D \|\Delta \boldsymbol{v}\|^2 + 2K_P K_D \|\Delta \boldsymbol{r}\| \|\Delta \boldsymbol{v}\| \end{aligned} \tag{33}$$

The parameter K_L in Eq. (33) appears in the matrix $\boldsymbol{P}$ used to obtain Eqs. (28) and (30), as shown in the Appendix. Combining Eqs. (25), (32), and (33) yields the desired expression:

$$K_L \|\Delta \boldsymbol{r}\|^2 + K_D \|\Delta \boldsymbol{v}\|^2 - 2K_P K_D \|\Delta \boldsymbol{r}\| \|\Delta \boldsymbol{v}\| \leq \|\delta \boldsymbol{u}\| T/(2\alpha m) \tag{34}$$

Deadband Region

The deadband in the thruster switching curve in Fig. 2 will result in exponential convergence to within a deadband region in the domain of $\boldsymbol{x}$ determined by the parameter ε in Eq. (29). Using Eqs. (27), (29), and (33), one can obtain the following expression for this region:

$$\begin{aligned} K_L \|\Delta \boldsymbol{r}\|^2 + K_D \|\Delta \boldsymbol{v}\|^2 - 2K_P K_D \|\Delta \boldsymbol{r}\| \|\Delta \boldsymbol{v}\| \\ \leq [\varepsilon + 3\|\delta \boldsymbol{u}\|] T/(4\alpha m) \end{aligned} \tag{35}$$

Exponential Convergence Region

From Eq. (26), it is evident that the parameter E is no longer bounded when the commanded thrust vector exceeds the capability

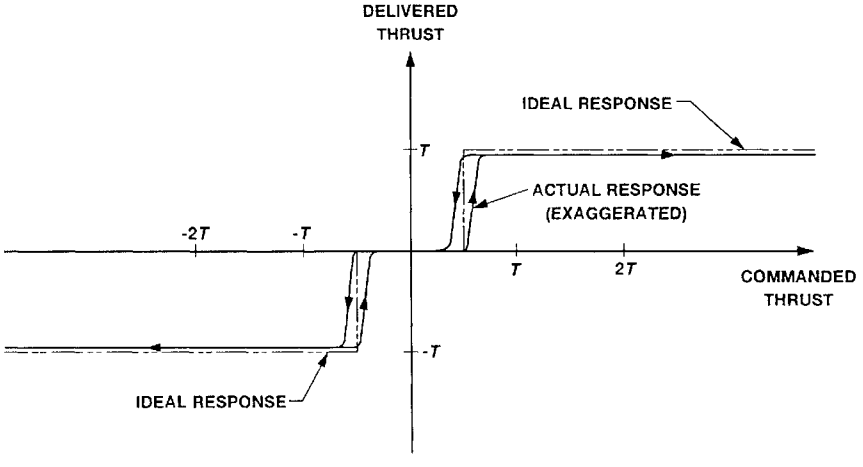

Fig. 2 Switching curve for reaction control system.

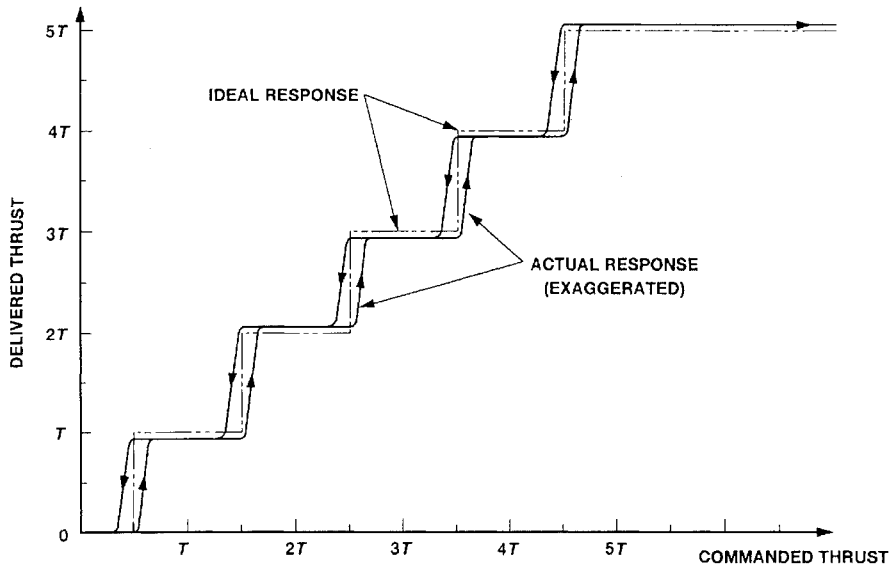

Fig. 3 Switching curve for clustered engine configuration.

of the propulsion system (i.e., saturation). Beyond this point, exponential convergence cannot be assured. Assuming that the effects of navigation errors are relatively small, this region is defined by

$$m(\|\ddot{\boldsymbol{r}}_d\| + \|\boldsymbol{g}\| + \|\boldsymbol{c}\| + K_P\|\Delta\boldsymbol{r}\| + K_D\|\Delta\boldsymbol{v}\|) \leq T_{\max} \tag{36}$$

In Eq. (36), $T_{\max}$ represents the maximum thrust capability of the propulsion system. In some cases, especially rendezvous applications, the functions $\boldsymbol{g}$ and $\boldsymbol{c}$ can be functions of $\Delta\boldsymbol{r}$ and need to be represented as such to obtain a useful expression.

Asymptotic Convergence Region

The minimum requirement for assuring convergence of the state trajectories to within the deadband region, regardless of rate, is to have $\dot{V}(\boldsymbol{x}) < 0$. Using Eqs. (25), (26), and (33), one obtains the following inequality describing this constraint:

$$\begin{aligned}&\left(K_P^2 - \alpha K_L\right)\|\Delta\boldsymbol{r}\|^2 + K_D(K_D - \alpha)\|\Delta\boldsymbol{v}\|^2\\&\quad + 2K_PK_D(1+\alpha)\|\Delta\boldsymbol{r}\|\|\Delta\boldsymbol{v}\|\\&\quad + (K_P\|\Delta\boldsymbol{r}\| + K_D\|\Delta\boldsymbol{v}\|)(\|\boldsymbol{a}_O\| - T_{\max}/m) \leq 0\end{aligned} \tag{37}$$

In Eq. (37), the term $\|\boldsymbol{a}_O\|$ is equal to $\|\boldsymbol{g}\| + \|\boldsymbol{c}\| + \|\ddot{\boldsymbol{r}}_d\|$. The potential dependence of the functions $\boldsymbol{g}$ and $\boldsymbol{c}$ on $\Delta\boldsymbol{r}$ must be taken into account in this case as well.

Clustered Engine Configuration

Spacecraft that must perform relatively large (>100-m/s) velocity changes may be equipped with multiple engines in a clustered arrangement to provide an operating range of several discrete thrust levels. In this case the thrusters would likely be mounted parallel to one another. With this configuration, the thrust axis must be continually aligned by the attitude control system with the commanded thrust vector.

Guidance Law

The relationship between the commanded and applied thrust along the thrust axis is shown in Fig. 3, including the actual response of typical thrusters. The function $\boldsymbol{n}$ in this case is chosen to be a variant of the saturation function:

$$\begin{aligned}\boldsymbol{n}(\varepsilon, \hat{\boldsymbol{u}}) &= \hat{\boldsymbol{u}}/\varepsilon; \qquad \|\hat{\boldsymbol{u}}\| < \epsilon\\ \boldsymbol{n}(\varepsilon, \hat{\boldsymbol{u}}) &= \hat{\boldsymbol{u}}/\|\hat{\boldsymbol{u}}\|; \qquad \|\hat{\boldsymbol{u}}\| \geq \varepsilon\end{aligned} \tag{38}$$

This form of $\boldsymbol{n}$ avoids step changes in the orientation of the commanded thrust vector, which could destabilize the operation of the spacecraft's attitude control system. As shown in Fig. 3, the maximum error between the commanded and applied thrust along the thrust axis, before saturation, is $0.5T$, where T is again the thrust level of a single thruster. As the thrust level quantization error in each component of the guidance coordinate frame is a function of the commanded thrust vector orientation, a modified version of the commanded thrust expression of Eq. (31) is proposed for this case, which is tailored to the characteristics of the thrust mechanization errors:

$$\boldsymbol{f}_c = \boldsymbol{f}_O + \boldsymbol{f}_f - (T/2)\boldsymbol{K}_\varepsilon\boldsymbol{n}[(1/\varepsilon)(K_P\Delta\hat{\boldsymbol{r}} + K_D\Delta\hat{\boldsymbol{v}})] \tag{39}$$

where

$$\boldsymbol{f}_O + \boldsymbol{f}_f = m(\ddot{\boldsymbol{r}}_d - \hat{\boldsymbol{g}} - \hat{\boldsymbol{c}} - K_P\Delta\hat{\boldsymbol{r}} - K_D\Delta\hat{\boldsymbol{v}}) \tag{40}$$

and

$$\boldsymbol{K}_\varepsilon = \begin{bmatrix} k_O + \sin|\theta| & 0 & 0\\ 0 & k_O + \sin|\phi| & 0\\ 0 & 0 & k_O + \cos\sqrt{\theta^2 + \phi^2}\end{bmatrix} \tag{41}$$

In Eq. (39), the function $\boldsymbol{n}$ is that of Eq. (38). The commanded thrust components seen in Eq. (40) are unchanged from their counterparts in Eq. (31). The parameters θ and ϕ appearing in Eq. (41) are the angles between the z axis of the guidance coordinate frame and the projections of the thrust vector in the x–z plane and the y–z plane, respectively. The parameter k_O must be greater than zero and must be chosen to ensure that norm of the matrix $\boldsymbol{K}_\varepsilon$ satisfies Eq. (18); if k_O were equal to zero, this might not otherwise be the case when the angles θ and ϕ are close to zero.

Performance Analysis

With the guidance law proposed earlier, the sensor uncertainty region, deadband region, exponential convergence region, and asymptotic convergence region can be characterized by the same equations derived for the reaction control system. These are Eqs. (34–37), respectively. Note that the use of these equations for the clustered engine configuration will generally lead to conservative results, since it is assumed that the thrust mechanization errors in each coordinate have their maximum possible value, regardless of the commanded thrust vector orientation. In terminal descent and landing applications, the thrust magnitude needed to compensate for the gravitational pull of the target body may result in at least one thruster firing continuously. The use of the phrase deadband region in this case is not meant in the literal sense.

Mars Soft Landing Computer Simulation

In this section the guidance theory presented earlier is applied to the conceptual design of an integrated guidance, navigation, and

control system for a hypothetical Martian soft lander. The performance of this vehicle is then investigated with a detailed digital computer simulation.

Mission and Spacecraft Description

The mission profile is illustrated in Fig. 1. The lander is transported to Mars in an entry vehicle that is carried by a cruise stage, which supports power generation, telecommunication, attitude determination and control, and midcourse propulsion functions during the interplanetary phase of the flight. The principal element of the lander's guidance system is an inertial navigation system, whose state vector is initialized 34 min before landing ($L - 34$ min in Fig. 1) with ground-based estimates of the spacecraft position and velocity vectors. The attitude matrix of the guidance system is established by an alignment process performed onboard the spacecraft. The alignment process is also used to calibrate the bias error components of the system's gyroscopes and accelerometers.

After initialization, the cruise stage's reaction control system is used to perform small maneuvers, correcting any discrepancies between the flight path indicated by the guidance system and a stored trajectory profile, and for three-axis attitude control. Shortly before atmospheric entry, the entry vehicle is spun up to 2 rpm by the cruise stage, which is then jettisoned. As the Martian surface approaches, a parachute is deployed to further slow the lander, and an onboard radar altimeter is activated. Once the radar system locks on to the surface, the lander separates from the entry vehicle backshell, activates its propulsion system, and completes its descent under automatic control. This mission profile is based on the entry and descent sequence for the Mars Pathfinder robotic spacecraft.[24] Unlike the guided lander simulated herein, Mars Pathfinder is an unguided vehicle that employs solid rocket motors for braking shortly before landing, yielding impact velocities of 10–30 m/s; the vehicle cushions itself from the landing shock using an airbag system.

Key configuration data for the lander are given in Table 1. The spacecraft's propulsion system is the clustered engine type of a configuration described previously. This system consists of seven 445-N main thrusters and four 4.5-N thrusters for roll control. The thrusters employ hypergolic nitrogen tetroxide/hydrazine propellants delivered by a blowdown pressurization system and are based on actual prototype hardware developed for small interceptor vehicles designed to destroy ballistic missiles.[25] By differential pulsing of engines offset from the nominal thrust axis, attitude control about the pitch and yaw axes is accomplished with the same thruster set used for guidance.

A high-level block diagram of the guidance, navigation, and control system is shown in Fig. 4. The spacecraft is equipped with a strapdown inertial measurement unit (IMU), consisting of three ring-laser gyroscopes and three pendulous integrating accelerometers, and a small radar altimeter. The inertial instrument data are processed to mechanize the landing site-centered rotating coordinate frame of Fig. 1 in the spacecraft's flight computer, yielding indicated position, velocity, and attitude data (these quantities are designated with a subscript i in Fig. 4), which, along with a radar bias error parameter, are corrected by a sequential filter algorithm that processes altitude measurements from the radar system. The radar is a wide beamwidth (60-deg) first-return unit; that is, it measures the distance from the vehicle to the nearest point on the surface. The estimated position, velocity, and attitude parameters (indicated by a hat symbol in Fig. 4) are used by the guidance law to compute the commanded thrust vector magnitude and orientation, designated f_c and Θ_c, respectively, in Fig. 4. The commanded thrust vector orientation is then passed to the attitude control law for determination of the commanded moment vector, designated $\boldsymbol{m}_c$ in Fig. 4. The jet select logic in the engine controller issues firing commands to specific thrusters based on the values of $\boldsymbol{m}_c$ and f_c.

Using Eqs. (38–41), a guidance law for the lander was developed. The switching curve of Fig. 3 (for a cluster of seven engines instead of the five shown) was used by the engine controller. The elements of the matrix function $\boldsymbol{K}_\varepsilon$ appearing in Eq. (41) were chosen to compensate for thrust mechanization errors as a result of the operation of the attitude control law, in addition to thrust level quantization errors in the switching curve of Fig. 3. An attitude control law with the same form as Eq. (31) was developed, with the appropriate terms from the rotational equations of motion substituted for the gravitational and Coriolis acceleration terms (the functions $\boldsymbol{g}$ and $\boldsymbol{c}$, respectively),

Table 1 Mars lander spacecraft configuration data

Parameter	Nominal value	RMS (1σ) variation, %
Initial mass		
Spacecraft (dry), kg	220.0	±1.0
Propellant/oxidizer, kg	30.0	±1.0
Initial moments of inertia		
Yaw (x axis), kg-m^2	80.0	±2.0
Pitch (y axis), kg-m^2	80.0	±2.0
Roll (z axis), kg-m^2	100.0	±2.0
Center of mass offset, cm	0.0	±1.0
Main thrusters		
Thrust level, N	445.0	±3.0
Rise time, ms	3.0	——
Max acceleration, m/s^2	12.5	——
Max pitch/yaw acceleration, rad/s^2	1.11	——
Roll thrusters		
Thrust level, N	4.45	±3.0
Rise time, ms	1.0	——
Max roll acceleration, rad/s^2	0.10	——

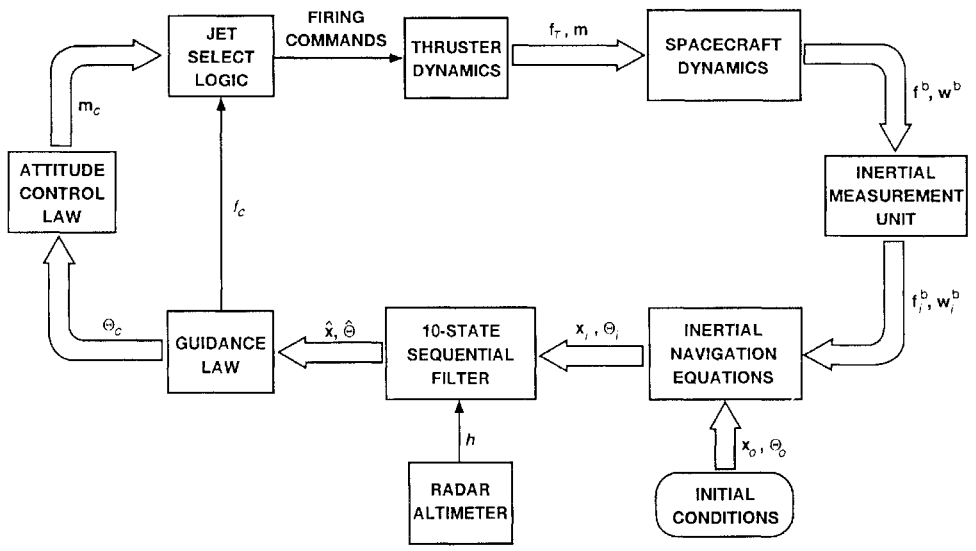

Fig. 4 Mars lander guidance, navigation, and control system. f_T = thruster vector, m = moment vector, f^b = contact force in body frame, w^b = angular velocity in body frame, x = spacecraft state (position, velocity), Θ = spacecraft attitude parameters, and h = measured altitude.

Table 2 Guidance and control system parameters

Parameter	Description	Value
Computer cycle rate, Hz	Frequency of command computations	50
Delay time, ms	Computation time required for each command computer cycle	3
Guidance law		
α, s^{-1}	Guidance error rate of convergence	10
Q_P, s^{-2}	Position weighting factor	10^{-5}
Q_D	Velocity weighting factor	10^{-5}
K_D, s^{-1}	Velocity feedback gain	0.2
K_P, s^{-2}	Position feedback gain	0.02
K_L, s^{-3}	Lyapunov function parameter	0.004
k_O	Corrective scale factor	0.05
ε, m/s^2	Guidance deadband parameter	0.02
Attitude control law		
α, s^{-1}	Attitude error rate of convergence	1
Q_P, s^{-2}	Angular position weighting factor	10^{-5}
Q_D	Angular rate weighting factor	10^{-5}
K_D, s^{-1}	Angular rate feedback gain	4.0
K_P, s^{-2}	Angular position feedback gain	8.0
K_L, s^{-3}	Lyapunov function parameter	48
k, s^{-2}	Corrective acceleration (pitch/yaw)	1.11
k_r, s^{-2}	Corrective acceleration (roll)	0.10
ε, s^{-2}	Attitude deadband parameter	0.07

Table 3 Inertial navigation system error model

Parameter	RMS (1σ) value
Landing site elevation error, m	300
Initial position error, km	5.18 (altitude)
	7.55 (downrange)
	1.04 (crossrange)
Initial velocity error, m/s	6.36 (altitude)
	1.13 (downrange)
	1.96 (crossrange)
Initial attitude error, deg	0.33 (each axis)
IMU misalignment, arcsec	18
Gyro error model	
Bias calibration error, deg/h	0.10
Time-varying bias,[a] deg/h	0.03
Scale factor error, ppm	100
Time-varying scale factor,[a] ppm	25
Scale factor asymmetry, ppm	10
Time-varying asymmetry,[a] ppm	10
Random walk, $deg/h^{1/2}$	0.10
Accelerometer error model	
Bias calibration error, μg	50
Scale factor error, ppm	100
Scale factor asymmetry, ppm	25
Compliance (g^2), $\mu g/g^2$	1.0
White noise, mm/s	1.0
Radar altimeter error model	
Proportional bias[b]	0.003
White noise, m	0.20

[a]Modeled as first-order Gauss–Markov processes with time constants of 1 h.
[b]Modeled as first-order Gauss–Markov process with time constant of 3 min.

and angular position and velocity feedback terms substituted for the translational position and velocity terms of Eq. (31). The guidance and attitude control law parameter values are summarized in Table 2. The feedback gains given in Table 2 were obtained by solution of Eq. (A3) in the Appendix. Command force and moment values were computed and transmitted to the engine controller every 20 ms, as indicated in Table 2. The engine controller issues commands to the thruster valves only when it detects a change in the requested state of a given thruster.

The error model for the inertial navigation system is summarized in Table 3. The instrumentation errors are represented by mathematical models developed through extensive test and flight experience.[26] The performance of this system is representative of similar systems used in short-range military aircraft and guided missiles. The initial position and velocity uncertainties represent the error covariance of the navigation system after propagation of the error covariance matrix at initialization, determined by Earth-based radio tracking of the spacecraft, along the atmospheric entry trajectory to the point of radar lock-on. (Britting[27] provides a detailed treatment of the error equations for inertial navigation systems.) Navigational errors were simulated by numerical integration of the error equations, using a pseudorandom number generator to sample the statistical distributions of the error sources described in Table 3. It is assumed that the inertial navigation equations are implemented in the flight computer with sufficient accuracy to make numerical computation errors negligible.

Simulation Procedure

At radar lock-on, the target landing site is designated to be the point directly below the lander. This results in the radar system viewing the same terrain during most of the descent, minimizing the effects of unknown terrain variations in the altitude data. If the commanded thrust vector has a positive z component (which can occur early in the descent), requiring the spacecraft to accelerate towards the surface, this component is ignored, and instead only the gravity compensation component is implemented, allowing the lander to continue at its current rate of descent. The guidance law uses constant values of $\boldsymbol{r}_d$ and $\dot{\boldsymbol{r}}_d$, chosen to target the spacecraft to a descent rate of 2 m/s at an altitude of 10 m. Once the spacecraft approaches these values to within the prescribed deadband region, the x and y target coordinates are reset to the current x and y position values indicated by the navigation system, to remove the effects of position errors from the commanded thrust vector, and a target altitude and descent rate of 0 m and 1 m/s, respectively, are commanded until touchdown occurs. This final descent segment is designed to minimize the lateral velocity of the lander at touchdown.

In vertical descent the resulting closed-loop system is characterized by one-axis dynamic behavior given by

$$\Delta\ddot{r} + k_D\Delta\dot{r} + k_P\Delta r = 0 \tag{42}$$

Using the values of gains computed using the proposed approach results in a closed-loop damping $\zeta = 0.707$ and a natural frequency $\omega = 1.414\alpha$. For a detailed description of the approach to one-axis guidance and attitude control given, see Ref. 21.

Results

Results obtained from simulations representing three different scenarios are summarized next. The x and y components of initial position were zero in all cases. The lander is also assumed to be in a vertical orientation initially in each case. Case 1 represents an ideal scenario in which radar lock-on is achieved at a nominal 1500-m altitude and 70-m/s descent rate (see Fig. 1), with the lander having no initial downrange (x) or crossrange (y) velocity components. Case 2 represents a scenario in which radar lock-on occurs at an unexpectedly low altitude of 1100 m, and the lander has developed a 20-m/s downrange velocity on the parachute. Case 3 represents a worst case scenario in which the lander achieves radar lock-on at the nominal altitude but has developed unusually large downrange (40-m/s) and crossrange (30-m/s) velocity components while on the parachute and also has a relatively large descent rate of 80 m/s.

Contours defining the inaccessible, deadband, exponential convergence, and asymptotic convergence regions for the guidance law were developed using expressions based on Eqs. (34–37) and the data in Tables 2 and 3, and they are shown in a two-dimensional space spanned by $\|\Delta\boldsymbol{r}\|$ and $\|\Delta\boldsymbol{v}\|$ in Fig. 5. Curves representing the actual trajectories obtained in the three simulation cases are also shown in Fig. 5. The velocity coordinate histories for case 3, the worst case scenario, are shown in Fig. 6. The depression angle relative to the $-z$ axis and the azimuth angle relative to the x axis of the commanded and actual thrust vectors for case 3 are illustrated in Fig. 7. The commanded and actual thrust magnitude histories for case 3 are shown in Fig. 8.

The lander required about 40 s to reach the surface in each scenario. The velocity component histories of Fig. 6 are representative of the response of a linear system, demonstrating that the pulse modulation guidance law does, in fact, yield the desired type of closed-loop behavior. In addition, Figs. 6–8 show that simultaneous

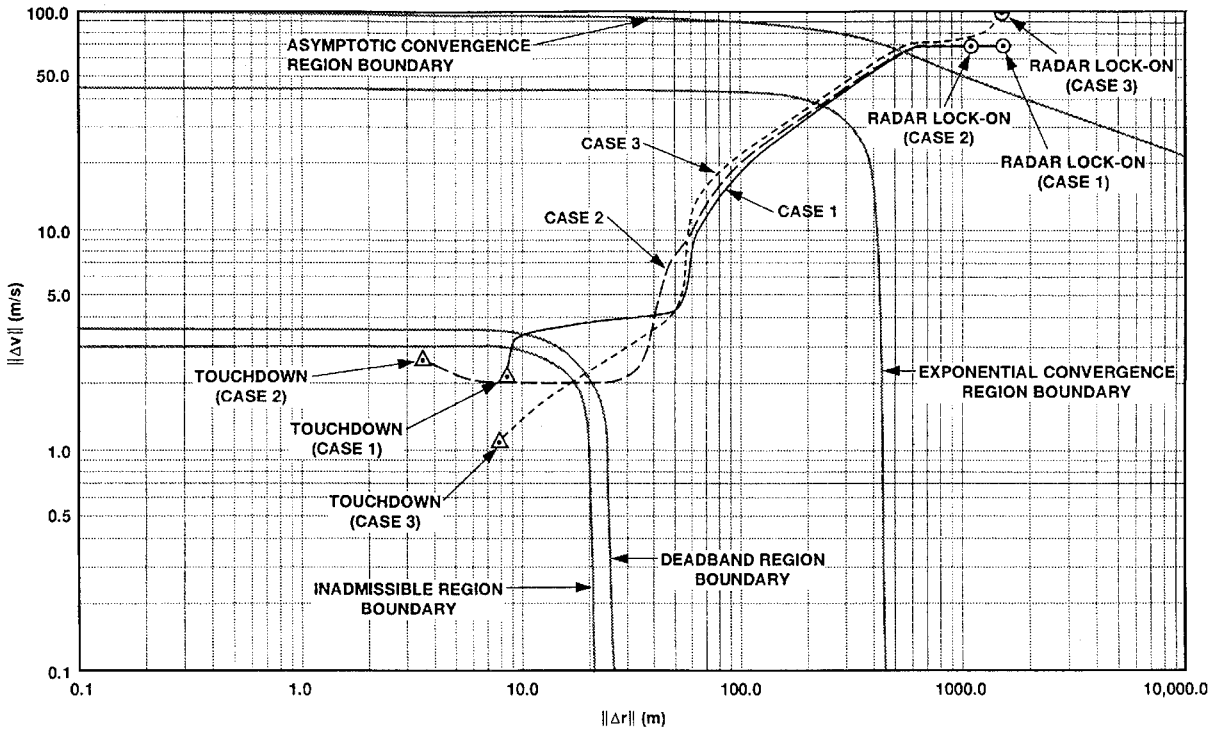

Fig. 5 Position–velocity magnitude map of simulation cases.

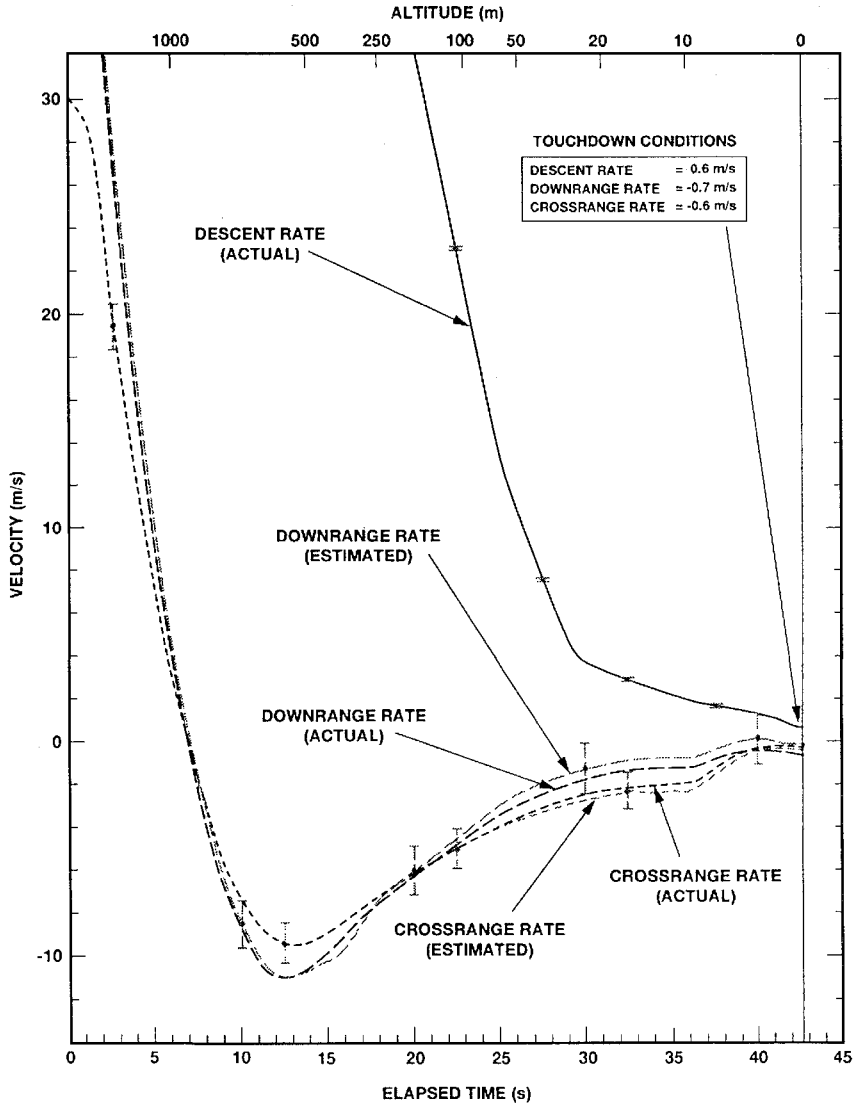

Fig. 6 Velocity vector components (simulation case 3). Note: error bars represent $\pm 1\sigma$ deviations.

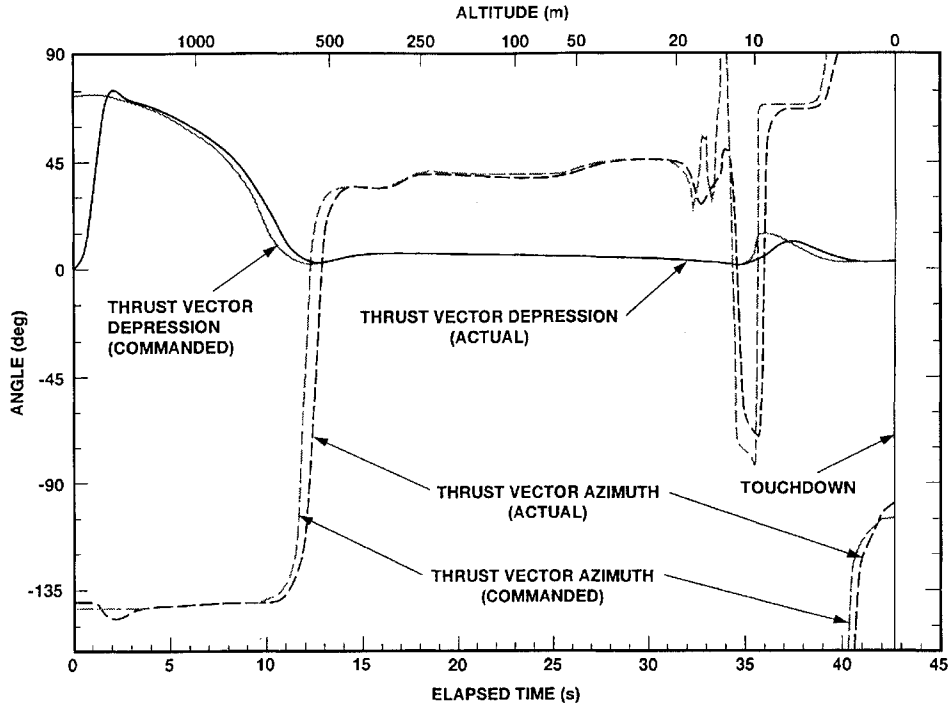

Fig. 7 Thrust vector orientation (simulation case 3).

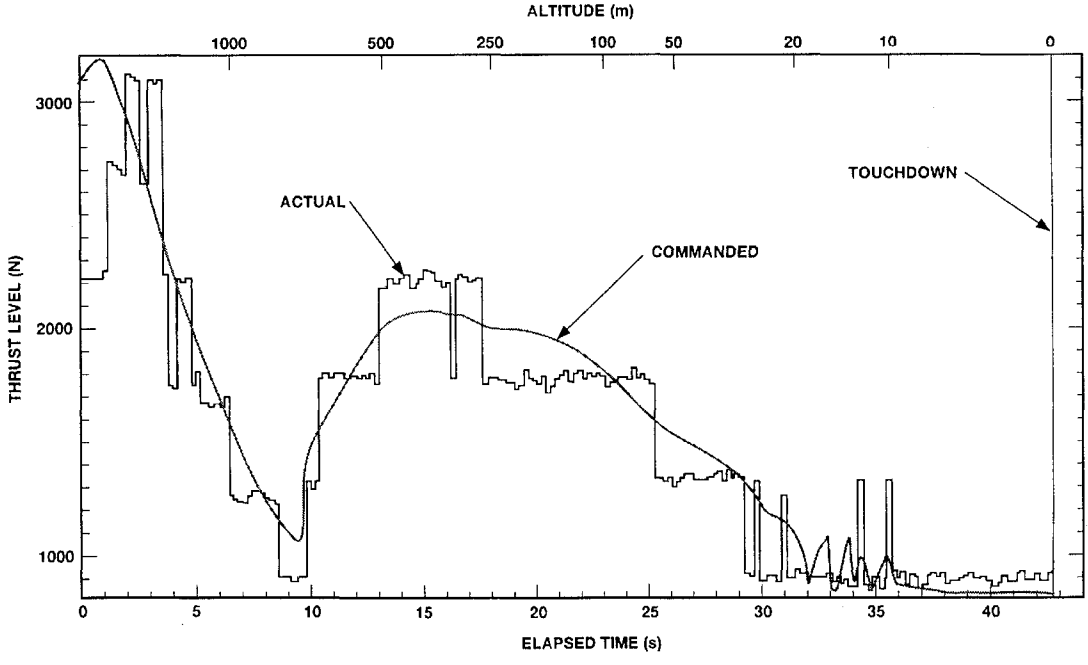

Fig. 8 Thrust magnitude (simulation case 3).

control of the lander's translational and rotational motion can be successfully achieved with the same thruster set. The thrust vector orientation history of Fig. 7 shows that the guidance law initially commands a large pitch maneuver to null the downrange and crossrange velocity components quickly. Although radar contact with the surface is lost for thrust vector depression angles greater than 30 deg, the lander quickly recovers to a near-vertical orientation for the remainder of the descent, ensuring proper radar operation. The erratic behavior of the thrust vector azimuth angles in Fig. 7 occurs because this parameter becomes undefined as the depression angle approaches zero. Note that when the first target altitude of 10 m is reached and the lander redesignates the x and y position components of its target state, the guidance law briefly commands a roughly 15-deg pitch maneuver. The effect of this maneuver can also be seen in Fig. 6. This occurs because the guidance system is nulling small downrange and crossrange velocity components that developed earlier, as a result of the buildup of x and y position errors in the inertial navigation system that could not be sensed by the sequential filter from the altimeter data.

Note from Fig. 5 that in all three scenarios the initial conditions lie outside the asymptotic convergence region and that the touchdown conditions are inside the "inadmissible" region. These characteristics serve to emphasize that Lyapunov theory establishes sufficient, not necessary, conditions for these regions. In general, the simulation results of Figs. 5–8, along with additional simulation results not included herein, suggest that bounds on the behavior of the guidance and control systems derived using Lyapunov-based design techniques tend to be conservative.

Conclusions

A new class of pulse-mode controllers for guidance and attitude control of spacecraft was developed. The proposed control algorithms were developed using Lyapunov's stability theory and result in a robust, exponentially convergent closed-loop behavior. These control laws are able to approximate a well-behaved, damped quasi-linear system by modulating both the width and frequency of jet pulses. The proposed approach does not depend on analytic approximations and allows for analytical characterization of closed-loop behavior in terms of important design parameters such as transient errors, limit cycle deadband region, and guaranteed region of convergence. Since Lyapunov's theory yields only sufficient conditions, the actual regions of convergence and transient behavior might be even better than predicted by the theory presented in this paper. The actual full capability of the proposed control laws needs to be eventually checked by simulation. However, as shown in a simulation study presented in this paper, the analytical conditions derived using the proposed approach lead to a very good qualitative assessment of the system's closed-loop behavior. This makes the proposed approach valuable in developing pulse-mode controllers whose behavior was evaluated exclusively by extensive numerical simulations.

Appendix: Feedback Gain Matrix Computation

One useful technique for matching the feedback components of the commanded thrust, the vectors $\boldsymbol{f}_f$ and $\boldsymbol{f}_\varepsilon$ from Eqs. (7) and (8), respectively, is to set the gain matrix $\boldsymbol{K}$ in Eq. (7) equal to $\boldsymbol{B}^T\boldsymbol{P}\boldsymbol{x}$. As shown by Corless,[20] this yields the following matrix Riccati equation:

$$\boldsymbol{P}[\boldsymbol{A}+\alpha\boldsymbol{I}]+[\boldsymbol{A}+\alpha\boldsymbol{I}]^T\boldsymbol{P}-2\boldsymbol{P}\boldsymbol{B}\boldsymbol{B}^T\boldsymbol{P}+2\boldsymbol{Q}=\boldsymbol{0} \tag{A1}$$

The matrices $\boldsymbol{A}$ and $\boldsymbol{B}$ are given in Eq. (4). A class of solutions to Eq. (A1) has the following simple form:

$$\boldsymbol{P}=\begin{bmatrix} K_L\boldsymbol{I} & K_P\boldsymbol{I} \\ K_P\boldsymbol{I} & K_D\boldsymbol{I} \end{bmatrix} \tag{A2}$$

The matrix $\boldsymbol{Q}$ used to obtain solutions conforming to Eq. (A2) is as follows:

$$\boldsymbol{Q}=\begin{bmatrix} Q_P\boldsymbol{I} & \boldsymbol{0} \\ \boldsymbol{0} & Q_D\boldsymbol{I} \end{bmatrix} \tag{A3}$$

Substitution of Eqs. (A2) and (A3) into Eq. (A1) yields polynomial equations for K_D, K_P, and K_L:

$$\begin{aligned} &K_D^4-4\alpha K_D^3+\left(5\alpha^2-2Q_D\right)K_D^2+2\alpha\left(2Q_D-\alpha^2\right)K_D \\ &\quad+\left(Q_D^2-2\alpha^2Q_D-Q_P\right)=0 \\ &K_P=\alpha(K_D-\alpha)+\sqrt{\alpha^2(K_D-\alpha)^2+Q_P} \\ &K_L=2K_P(K_D-\alpha) \end{aligned} \tag{A4}$$

Although multiple solutions to Eq. (A4) exist, only one set of gains results in $\boldsymbol{P}$ being positive definite. For the correct solution, K_D, K_P, and K_L, as well as the expression $K_LK_D-K_P^2$, must be positive. As discussed earlier, the norm of the six-dimensional guidance error vector decreases exponentially with rate α. Within the exponential envelope established by a given α, the coefficients Q_P and Q_D appearing in Eq. (45) determine the amount of emphasis the resulting guidance law will place on nulling guidance errors in position relative to guidance errors in velocity.

Acknowledgments

The research described in this paper was carried out, in part, at the Jet Propulsion Laboratory (JPL), California Institute of Technology, under contract with NASA. The authors extend their thanks to Stephen Bailey of JPL for developing the Mars lander spacecraft configuration and to David Spencer, also of JPL, for providing the Mars Pathfinder entry trajectory data used in the digital computer simulations.

References

[1]Jezewskii, O. J., Brazzel, J. P., Jr., Prust, E. E., Brown, B. G., Mulder, T. A., and Wissinger, O. B., "A Survey of Rendezvous Trajectory Planning," *Advances in the Astronautical Sciences*, Vol. 76, Pt. II, Univelt, San Diego, CA, 1992, pp. 1373–1396.

[2]Leonard, C. L., and Bergmann, E. V., "A Survey of Rendezvous and Docking Issues and Developments," *Advances in the Astronautical Sciences*, Vol. 69, Univelt, San Diego, CA, 1989, pp. 85–101.

[3]Parten, R. P., and Mayer, J. P., "Development of the Gemini Operational Rendezvous Plan," *Journal of Spacecraft and Rockets*, Vol. 5, No. 9, 1968, pp. 1023–1028.

[4]Young, K. A., and Alexander, J. D., "Apollo Lunar Rendezvous," *Journal of Spacecraft and Rockets*, Vol. 7, No. 9, 1970, pp. 1083–1086.

[5]Olszewski, O. W., "Automated Terminal Guidance for a Shuttle Rendezvous to Space Station Freedom," *Proceedings of the AIAA Guidance, Navigation, and Control Conference*, Vol. 1, AIAA, Washington, DC, 1990, pp. 377–387.

[6]Hanson, J. M., and Deaton, A. W., "Guidance Schemes for Automated Terminal Rendezvous," AAS/AIAA Spaceflight Mechanics Meeting, AAS Paper 94-163, Cocoa Beach, FL, Feb. 1994.

[7]Cherry, G. W., "A Class of Unified Explicit Methods for Steering Throttleable and Fixed-Thrust Rockets," *Guidance and Control—II*, edited by R. C. Langford, Vol. 13, Progress in Astronautics and Aeronautics, Academic, New York, 1964, pp. 689–726.

[8]Battin, R. H., *An Introduction to the Mathematics and Methods of Astrodynamics*, AIAA Education Series, AIAA, New York, 1987, pp. 550–566.

[9]Klumpp, A. R., "Apollo Lunar Descent Guidance," *Automatica*, Vol. 10, No. 1, 1974, pp. 133–146.

[10]Cheng, R. K., Meredith, C. M., and Conrad, D. A., "Design Considerations for Surveyor Guidance," *Journal of Spacecraft and Rockets*, Vol. 3, No. 11, 1966, pp. 1569–1576.

[11]Ingoldby, R. N., "Guidance and Control System Design of the Viking Planetary Lander," *Journal of Guidance and Control*, Vol. 1, No. 3, 1978, pp. 189–196.

[12]Farrenkopf, R. L., Sabroff, A. E., and Wheeler, P. C., "Integral Pulse Frequency On-Off Control," *Guidance and Control—II*, edited by R. C. Langford, Vol. 13, Progress in Astronautics and Aeronautics, Academic, New York, 1964, pp. 185–230.

[13]Widnall, W. S., "Lunar Module Digital Autopilot," *Journal of Spacecraft and Rockets*, Vol. 8, No. 1, 1971, pp. 56–62.

[14]Bergmann, E. V., Croopnick, S. R., Turkovich, J. J., and Work, C. C., "An Advanced Spacecraft Autopilot Concept," *Journal of Guidance and Control*, Vol. 2, No. 3, 1979, pp. 161–168.

[15]Corless, M., "Control of Uncertain Nonlinear Systems," *Journal of Dynamic Systems, Measurement and Control*, Vol. 115, June 1993, pp. 362–372.

[16]Leitmann, G., "On One Approach to the Control of Uncertain Systems," *Journal of Dynamic Systems, Measurement and Control*, Vol. 115, June 1993, pp. 373–380.

[17]Utkin, V. I., *Sliding Modes and Their Application to Variable Structure Systems*, Mir Publishers, Moscow, 1978.

[18]Slotine, J. J., and Li, W., *Applied Nonlinear Control*, Prentice–Hall, Englewood Cliffs, NJ, 1991.

[19]Vidyasagar, M., *Nonlinear Systems Analysis*, 2nd ed., Prentice–Hall, Englewood Cliffs, NJ, 1993.

[20]Corless, M., "Guaranteed Rates of Exponential Convergence for Uncertain Systems," *Journal of Optimization Theory and Applications*, Vol. 64, No. 3, 1990, pp. 481–494.

[21]Thurman, S. W., "A Comprehensive Guidance and Control Theory for Spacecraft Using Pulse Modulated Propulsion," Ph.D. Dissertation, Dept. of Aerospace Engineering, Univ. of Southern California, Los Angeles, CA, Aug. 1995.

[22]Brown, R. G., *Introduction to Random Signal Analysis and Kalman Filtering*, Wiley, New York, 1983.

[23]Thurman, S. W., and Flashner, H., "Application of Nonlinear Control Techniques to Spacecraft Guidance for Rendezvous and Docking," AAS/AIAA Spaceflight Mechanics Meeting, AAS Paper 94-166, Cocoa Beach, FL, Feb. 1994.

[24]Cook, R. A., "Mars Pathfinder Mission Plan," Jet Propulsion Lab., JPL Doc. D-11355 (internal document), California Inst. of Technology, Pasadena, CA, Dec. 1993.

[25]Acampora, K. J., and Wichmann, H., "Component Development for Micropropulsion Systems," AIAA Paper 92-3255, July 1992.

[26]Savage, P. G., "Strapdown Sensors," *Strapdown Inertial Systems*, NATO AGARD Lecture Series No. 95, Technical Information Service, Springfield, VA, June 1978.

[27]Britting, K. R., *Inertial Navigation Systems Analysis*, Wiley, New York, 1971, pp. 153–194.